

Nusrat Yussouf<sup>1</sup> and David J. Stensrud<sup>2</sup><sup>1</sup>Cooperative Institute for Mesoscale Meteorological Studies, Norman, Oklahoma<sup>2</sup>NOAA/National Severe Storms Laboratory, Norman, Oklahoma

## 1. INTRODUCTION\*

The new experimental research Phased Array Radar (PAR) built in 2003 at the National Weather Radar Testbed (NWRT) located in Norman, Oklahoma (Forsyth et al. 2004), provides unique opportunities for meteorologists to study rapidly evolving convective weather phenomena using more frequent volume updates. While the conventional Weather Surveillance Radar – 1988 Doppler (WSR-88D) radar typically takes slightly over 5 minutes to scan a thunderstorm, the emerging PAR rapid scanning technology can scan the same thunderstorm in less than a minute (Heinselman et al. 2008). However, an in-depth understanding of the PAR technology, including its strengths and limitations, is crucial to assessing its suitability as a replacement option for the current National Weather Service (NWS) WSR-88D radar network since the Doppler radar network is approaching the end of its engineered design 20-year life span.

A recent research application of the radial velocity and reflectivity observations provided by radar is their use in the initialization of storm-scale numerical prediction models using an ensemble Kalman filter (EnKF) data assimilation approach (Snyder and Zhang 2003; Zhang et al. 2004; Dowell et al. 2004a, b; Tong and Xue 2005, 2008; Caya et al. 2005; Xue et al. 2006; Jung et al. 2008; Aksoy et al. 2008). Results from these studies reveal that it is reasonable to expect at least 10 radar scans of WSR-88D observations are needed to produce reasonable analyses of storms. However part of the challenge in using 5-min radar observations to initialize thunderstorms in numerical models is that a

number of storm features evolve on a timescale of minutes and are poorly sampled by 5-min data. In addition, since accurate analyses require approximately 10 radar scans, the amount of time needed to obtain these scans from the WSR-88D is at least 45 min. However, the PAR can produce 10 radar scans in 10 min or less. Xue et al. (2006) show that the assimilation of synthetic 1-min radar data leads to analyses that more closely approach the truth solution than the analyses created using synthetic 5-min radar data. Similar results are found by Lei et al. (2007). Thus, it is reasonable to expect that PAR observations can generate accurate storm analyses very quickly. Moreover, a shorter assimilation period also is highly desirable in an operational environment if these analyses are to be used to increase warning lead times.

To quantitatively assess the impact of high temporal frequency PAR observations on storm-scale data assimilation, an obvious first step is to use an Observation System Simulation Experiment (OSSE) approach prior to working with real PAR observations. Therefore, several different OSSEs are conducted using synthetic radar observations from a simulated supercell storm as the reference, or truth, simulation. One experiment assimilates synthetic WSR-88D observations, in which a volume scan is conducted every 5 min, while the other experiment assimilates synthetic PAR observations, in which a volume scan is conducted every 1 min. The EnKF is used as the data assimilation method for both experiments with identical settings. The aim of this study is to assimilate radar data for a relatively short period of time (only 15 min) to determine how quickly and accurately the storm can be represented in the analyses. Other OSSEs are conducted to quantify the value of adaptive scanning capability of PAR.

---

\* *Corresponding author address:* Nusrat Yussouf, Cooperative Institute for Mesoscale Meteorological Studies, 120 David L. Boren Blvd. Norman, OK, 73072;  
e-mail: nusrat.yussouf@noaa.gov

## 2. EXPERIMENTAL DESIGN

The Collaborative Model for Multiscale Atmospheric Simulation (COMMAS; Wicker and Skamarock 2002, Coniglio et al. 2006) is used in this study to assess the impact of high temporal frequency PAR observations on EnKF analyses and forecasts. The COMMAS model is a nonhydrostatic compressible numerical cloud model with prognostic variables including the three velocity components,  $u$ ,  $v$ , and  $w$ ; pressure in the form of the perturbation Exner function,  $\pi$ ; potential temperature,  $\theta$ ; mixing coefficient  $k_m$ , and six categories of water substance, including water vapor,  $qv$ , cloud water,  $qc$ , rain water,  $qr$ , ice,  $qi$ , snow,  $qs$ , and hail/graupel,  $qh$  (Coniglio et al. 2008, Dowell and Wicker 2008). Both the truth simulation and EnKF analyses use the same 1-km horizontal grid resolution. The Gilmore et al. (2004) version of the Lin-Farley-Orville (Lin et al. 1983) single-moment bulk microphysics scheme is used for precipitation processes with four hydrometeor classes: rain, ice crystals, snow and hail/graupel. All the experiments in this study are conducted using a single radar to observe the supercell storm.

### *2.1. The truth simulation and synthetic radar observations*

The 2 h long truth simulation uses the classic Weisman-Klemp analytic sounding (Weisman and Klemp, 1982) with a quarter circle hodograph. An ellipsoidal thermal bubble of 2.5 K with 10 km radius in the horizontal direction and 1.4 km radius in the vertical direction is placed at the center of the domain to initiate a supercell thunderstorm at  $t = 0$  min. The model domain is 100 km long in the horizontal and 18 km long in the vertical direction. The domain is vertically stretched from 100 m vertical spacing at the bottom to 700 m vertical spacing at the domain top. The ellipsoidal thermal bubble develops into a convective cell within the first 30 min of the simulation and the first echo is seen by the radar emulator at around  $t = 25$  min. Over the next 1.5 h, the convective cell splits into two cells, one moving right towards the southeast and the other moving towards the

northwest and the right-moving cell tends to dominate the system with a few short lived smaller cells developing in between the two main cells. The domain grid is translated at  $u = 17$  and  $v = 7$   $\text{ms}^{-1}$  to keep the main storm near the center of the model domain.

Unlike previous OSSE studies that made simplifying assumptions regarding the radar observations (Synder and Zhang, 2003; Tong and Xue 2005; Xue et al. 2006; Jung et al. 2008), this study uses a radar emulator that generates radial-velocity and reflectivity observations from the reference simulation in native radar coordinates using a simplified version of a realistic volume averaging technique (Wood et al. 2008). The calculation of model reflectivity  $Z$  from model hydrometeors is similar to Coniglio et al. (2008). The  $Z$ ,  $u$ ,  $v$  and  $w$  wind components at model grid points within the beamwidth are scanned with the radar emulator to produce both WSR-88D and PAR radar reflectivity and radial velocity observations (Fig. 1). To reduce the heavy computational burden of observation assimilation, the reflectivity and radial velocity observations used in this study are created at a coarser 1.0-km range sampling interval instead of the 0.25 km interval available from the operational radars. The WSR-88D and PAR antenna half-power beamwidth is assumed to be  $0.89^\circ$  with  $1.0^\circ$  azimuth interval and a  $1.39^\circ$  effective beamwidth. The effects of the earth's curvature and bending of the radar beam far from the radar location (Doviak and Zrnic 1993) also are taken into consideration in calculating the radar observations.

To assimilate the WSR-88D observations more realistically, synthetic radar observations are generated for 2-3 sweeps every minute rather than assuming the entire volume (consisting of 14 elevation angle sweeps for Volume Coverage Pattern 11 precipitation mode scanning strategy) is collected simultaneously. Out of the 14 sweeps, the lower 12 sweeps of observations are generated 3 sweeps per minute for the first 4 min with the remaining upper 2 sweeps valid for the fifth minute of the volume scan. Observations for PAR data are generated instantaneously every minute for a complete volume scan. To account for the measurement and sampling errors for radial velocity and reflectivity observations, random numbers are drawn from a

Gaussian distribution of zero mean and standard deviations of  $2 \text{ ms}^{-1}$  and  $2 \text{ dBZ}$ , respectively, and are added to the observations. The radar reflectivity observations assimilated include non-precipitating observations as in Tong and Xue (2005) and Aksoy et al. (2008), while the radial velocity observations are assimilated only where the observed reflectivity values are greater than  $10 \text{ dBZ}$ .

## 2.2. The ensemble configuration

Each member of the 40 member ensemble uses the same classic Weisman-Klemp sounding with quarter circle hodograph in a horizontally homogeneous environment to define the initial environmental condition. To facilitate the development of storms, 7 thermal bubbles ( $1.5 \text{ K}$  maximum ellipsoidal  $\theta$  perturbations with  $7.5 \text{ km}$  radius in the horizontal direction and  $2.0 \text{ km}$  radius in the vertical direction) at random locations within the  $30 \text{ km}$  to  $70 \text{ km}$  portion of the domain in  $x$  and  $y$  directions and within  $0.25$  to  $2.25 \text{ km}$  in  $z$  direction are introduced at the initialization time ( $t = 0$ ) to each ensemble member following Snyder and Zhang (2003) and Dowell et al. (2004a, b). The ensemble members are then integrated forward in time for  $25 \text{ min}$  before the assimilation of first observations. During this time period, the ellipsoidal  $\theta$  perturbations initiate convective cells in the ensemble members (Snyder and Zhang 2003; Dowell et al. 2004a, b; Aksoy et al. 2008). The observations valid within  $1 \text{ min}$  of the current time are assimilated followed by advancing the ensemble members  $1 \text{ min}$  to the next observation time. Ensemble spread is maintained during these 60 assimilation cycles by adding spatially smoothed Gaussian perturbations every  $5 \text{ min}$  for WSR-88D observations assimilation and every  $2 \text{ min}$  for PAR observations assimilation to  $u$ ,  $v$ , and  $\theta$  with a standard deviation of  $1 \text{ ms}^{-1}$  and  $0.5 \text{ K}$ , respectively at locations where the observed reflectivity exceeds  $20 \text{ dBZ}$  (Dowell and Wicker, 2008). In addition, thermal ( $\theta$ ) perturbations are added to the members in locations where the observations indicate heavy precipitation and ensemble members do not. The thermal perturbations added are very similar to those created during initialization. The domain size and grid resolution for the ensemble

members are identical to the truth run. The domain of the ensemble also moves at  $u = 17$  and  $v = 7 \text{ ms}^{-1}$  following the truth run to keep the storm inside the domain. Moreover, while previous studies make a short term forecast initialized from the ensemble mean analysis at the last assimilation cycle (Snyder and Zhang 2003; Tong and Xue 2005), this study uses all of the 40 ensemble members at the last assimilation cycle to make a true ensemble forecast. Two sets of OSSEs are implemented in this study to assess the benefits and challenges of flexible and rapid update volumetric PAR data.

## 2.3. The OSSE design

### a. 15-min Assimilation

The first experiment assimilates radar observations for a 15-min period starting at  $t = 25 \text{ min}$  and ending at  $t = 39 \text{ min}$  using VCP 11 precipitation mode. During this 15-min assimilation period, 15 volume scans of PAR observations and 3 volume scans of WSR-88D observations are assimilated. After  $15 \text{ min}$  of data assimilation, the ensemble members are used to produce a  $50 \text{ min}$  forecast. The radar is located at  $x = 3.6 \text{ km}$  and  $y = 4.9 \text{ km}$  off of the southwest corner of the domain during the first volume scan.

### b. Enhanced PAR Scanning Strategies

In traditional WSR-88D VCP modes, the upper elevation angle of  $19.5^\circ$  often undershoots storm top height when a storm is very close to the radar location ( $\leq 35 \text{ km}$ ). Moreover, the spacing between elevation-angles above  $6^\circ$  (especially with VCP 11 scanning mode) often undersamples the vertical structure of storms. This is due to the vertical data gaps in radar coverage above  $6^\circ$  (Fig 2a). In contrast, when the storm is far away from the radar ( $> 70 \text{ km}$ ), scanning up to  $19.5^\circ$  from VCP 11 mode overshoots the storm top, while the lower levels of the atmosphere remain under sampled. With the PAR adaptive scanning capability, however, it is possible to enhance the scanning angles in real time when the storm is either close or far away from the radar. In an effort to determine how well the PAR adaptive scanning capability can be utilized to yield a better depiction of the

storm evolution, two enhanced VCP 11 scanning strategies with improved vertical sampling similar to the 2008 National Severe Storms Laboratory (NSSL) Real-time PAR Experiment ([http://www.nssl.noaa.gov/projects/pardemo/Spring08\\_PAR\\_Operations\\_Plan\\_Web.pdf](http://www.nssl.noaa.gov/projects/pardemo/Spring08_PAR_Operations_Plan_Web.pdf)) are used. The first enhanced scanning strategy adds six additional scans to the VCP 11 mode with elevation angles as high as  $23.70^\circ$  above ground when the storm is located very close to the radar location (Fig. 2b). These higher elevation angles sample the storm top that is unobserved when using the VCP 11 mode. The second enhanced scanning strategy adds several new lower elevation angles to better scan the lower levels of the atmosphere while removing higher elevation scans when the storm is far away from the radar (Fig. 2c). Thus, these enhanced VCP 11 scan strategies take advantage of the operational VCP 11's accuracy while improving the vertical sampling based on whether storms are near or far away from the radar. A list of the scan angles for the enhanced VCP-11 scanning is given in Table 1.

### 3. ANALYSIS RESULTS

The accuracy of the analyses and forecasts from PAR and WSR-88D observation assimilations are evaluated using both statistical and graphical comparison of the ensemble mean analyses and forecasts to the truth run. Statistical measures include the root-mean-square (rms) error of the unobserved variables, calculated as the difference between the reference simulation and the ensemble mean analyses averaged over only those model grid points where the total precipitation mixing ratio (sum of rain, snow and hail mixing ratios) is greater than  $0.10 \text{ g kg}^{-1}$ .

#### 3.1. 15-min Assimilation

The rms errors from both PAR and WSR-88D observation assimilations are seen to decrease rapidly for all variables (Fig. 3). However, the faster volume scans of PAR observation generates significantly smaller rms error compared to the WSR-88D assimilation for all variables. The reflectivity and vertical velocity structure of

the supercell storm in mid-levels from PAR observation assimilation more closely resembles the truth than that of the WSR-88D observation assimilation (Fig. 4). The PAR ensemble-mean analyses captures the location, structure and the strength of the two main precipitation cores as in the truth, while the WSR-88D analyses fail to capture the high-reflectivity core of the northern cell and barely captures the high-reflectivity core of the southern cell. In addition, while a number of spurious cells still surround the main supercell in the WSR-88D analyses, the more frequent observations assimilation from PAR suppresses most of the spurious convection. Furthermore, the two strong updrafts in excess of  $16 \text{ ms}^{-1}$  from the northern and southern cells (Fig. 4b) in the truth are well represented in the PAR analyses (Fig. 4d), while the WSR-88D analyses (Fig. 4f) fail to capture the location, structure and the strength of the updrafts. Similar results also are found for other variables at other vertical levels of the model domain. These results clearly show the benefit of assimilating faster volume scan observations for capturing the split supercell structure of the storm in the analyses resulting in a more accurate depiction of this simulated severe weather event.

#### 3.2. Enhanced PAR Scanning Analyses

To evaluate if the accuracy of the analyses is improved with the enhanced flexible scanning ability of PAR, the analyses with the enhanced scanned PAR observations are compared to those using the regular VCP 11 scanned PAR observation assimilation. Results indicate that when the storm is very close to the radar, the assimilation of enhanced PAR observations generates smaller rms errors for winds, temperature and precipitation variables compared to the rms errors from VCP 11 scanned PAR data (Fig 5). The reflectivity plots at 6.1 km AGL and valid at the last assimilation cycle at  $t = 39 \text{ min}$  show that the enhanced PAR analyses capture the split cell structure of the developing supercell (Fig. 6). Both the regular PAR (Fig. 6b) and WSR-88D (Fig. 6d) analyses also captures the storm structure. Moreover, the WSR-88D observations assimilation suppresses most of the spurious cell due to a large number of observations at close

range to storm location.

When the storm is far away from the radar location, the rms error for the enhanced PAR assimilation is slightly smaller in general than the regular PAR assimilation at the last assimilation cycle. However, the difference in the errors is not large. The reflectivity contours (Fig. 8) at 2.1 km AGL at the last assimilation cycle ( $t = 39$  min) from regular (Fig. 8b) and enhanced (Fig. 8c) PAR observation assimilation shows that the location, structure and the strength of the two main precipitation core closely match each other and both are more accurate than the WSR-88D analysis (Fig. 8d) when compared with the truth (Fig. 8a).

#### 4. FORECAST RESULTS

The ultimate goal of storm-scale data assimilation is to increase warning lead times by obtaining more accurate short term forecasts of severe storms events. Thus, to evaluate the accuracy of the forecasts from both PAR and WSR-88D observation assimilation, the ensemble mean forecasts are compared with the truth run. In contrast to most previous studies, the full ensemble is used to produce the forecasts instead of a single forecast from the ensemble mean analysis.

##### 4.1. Forecasts from 15-min Analyses

The rms errors of the ensemble mean forecasts show that the rms errors grow rapidly during the forecast period from both PAR and WSR-88D observation assimilation as expected (Fig. 9). However the forecast errors from PAR observation assimilation are significantly smaller than the forecast errors from WSR-88D observation assimilation for the entire 50-min forecast period. The reflectivity contours from the truth simulation and 5-min forecast at 6.1 km AGL and 20-min forecasts at 2.1 km from PAR and WSR-88D observation assimilation indicate that the forecasts from PAR observation assimilation maintains the strength, split storm cell structure and location of the two main precipitation core more closely to the truth than that of the WSR-88D forecasts (Fig. 10). Thus, the more accurate analyses from the PAR observation

assimilation yields better forecasts compared to the WSR-88D forecasts.

##### 4.2. Forecasts from Enhanced PAR Scanning Analyses

The ensemble mean forecast rms error from enhanced and regular scan PAR observation assimilation indicate that when the storm is very close to the radar location, both errors are similar to each other for all variables (Fig. 11). In contrast, when the radar is far away from the storm, the rms error from enhanced scan is smaller than the regular scan for almost the entire 50-min forecast period (Fig. 12).

#### 5. DISCUSSION

To explore the potential benefit of the PAR high temporal frequency radar observations in assimilating storms in storm-scale numerical weather prediction model and to compare its performance to that of the conventional WSR-88D observation assimilation, a set of OSSEs are conducted using synthetic PAR and WSR-88D radar observations in native radar coordinates. The synthetic reflectivity and radial velocity observations created from a truth simulation of a supercell storm are assimilated into a nonhydrostatic storm-scale model using an EnKF data assimilation technique. Additional OSSEs also are conducted to assimilate PAR observations from enhanced volume scans when the supercell storm is either very close to or far away from the radar location. Finally, the analyses and forecasts from rapid scan PAR observations assimilation are compared to that of WSR-88D observations.

The results indicate that the PAR observations provide more accurate analyses and forecasts of the simulated supercell thunderstorm compared to the WSR-88D data. There is a rapid increase in rms errors in both PAR and WSR-88D ensemble mean forecasts during the 50-min forecast period, but the errors for PAR observation assimilation are consistently smaller than for WSR-88D observation assimilation. Moreover improved analyses also are obtained from assimilating enhanced scanned volumes of PAR observations compared to that of the regular VCP 11 scans of PAR observations of the

same storm when the radar is either very close or far away from the radar location. While the ultimate goal of storm-scale data assimilation is to obtain accurate forecasts of severe weather events and is still a challenge to researchers, the good quality 3-D storm analyses from PAR assimilation likely can help forecasters make more accurate and timely warning decisions.

In general, the results show promise that high-temporal frequency radar observation assimilation may improve short-term forecasting and warnings of severe weather events with the possibility of increasing warning lead time from assimilating over a shorter period of time. However, the results obtained in these OSSE studies are based on a perfect model experiment and represents only the first step in this direction. A similar outcome is yet to be documented using real radar data. To lay a foundation for the new and emerging PAR technology beyond the current WSR-88D network in storm-scale modeling, a broader range of experiments needs to be conducted with real radar observations.

*Acknowledgments.* The authors are indebted to Vincent “Bim” Wood for his help with the volume averaging code. The authors also are grateful to Ted Mansell, David Dowell and Louis Wicker for help with the COMMAS model. Pamela Heinselman is thanked for sharing her knowledge of the phased array radar technology. Local computer assistance provided by Brett Morrow, Steven Fletcher, Brad Swagowitz, and Karen Cooper are greatly appreciated. Partial funding for this research was provided by NOAA/Office of Oceanic and Atmospheric Research under NOAA-University of Oklahoma Cooperative Agreement #NA17RJ1227, U.S. Department of Commerce.

## REFERENCES

Aksoy, A., D. Dowell, and C. Snyder, 2008: Ensemble Kalman filter assimilation of real radar observations: A multi-case comparative study of storm-scale forecasts and analyses. Submitted to *Mon. Wea. Rev.*

Caya, A., J. Sun, and C. Snyder, 2005: A Comparison between the 4DVAR and the Ensemble Kalman Filter Techniques

for Radar Data Assimilation. *Mon. Wea. Rev.*, **133**, 3081–3094.

Coniglio, M.C., D.J. Stensrud, and L.J. Wicker, 2006: Effects of upper-level shear on the structure and maintenance of strong quasi-linear mesoscale convective systems. *J. Atmos. Sci.*, **63**, 1231-1252.

\_\_\_\_\_, D.C. Dowell, and L.J. Wicker, 2008: Storm-scale ensemble Kalman filter analyses of a developing mesoscale convective system. *J. Atmos. Oceanic Technol.*, submitted.

Doviak, R. J. and D. S. Zrnic, 2006: *Doppler Radar and Weather Observations*. Dover Publications, 562 pp.

Dowell, D. C., and L. J. Wicker, 2008: Additive noise for storm-scale ensemble forecasting and data assimilation. Submitted to *J. Atmos. Oceanic Technol.*

\_\_\_\_\_, F. Zhang, L. J. Wicker, C. Snyder, and N.A. Crook, 2004a: Wind and temperature retrievals in the 17 May 1981 Arcadia, Oklahoma, supercell: Ensemble Kalman filter experiments. *Mon. Wea. Rev.*, **132**, 1982-2005.

\_\_\_\_\_, L. J. Wicker, and D. J. Stensrud, 2004b: High resolution analyses of the 8 May 2003 Oklahoma City storm. Part II: EnKF data assimilation and forecast experiments. Preprints, *22nd Conf. Severe Local Storms*, Hyannis, MA, Amer. Meteor. Soc.

Forsyth, D. E., and Coauthors, 2004: The National Weather Radar Testbed (phased-array) becomes operational. Preprints, *20th Int. Conf. on Interactive Information and Processing Systems (IIPS) for Meteorology, Oceanography, and Hydrology*, Seattle, WA, Amer. Meteor. Soc., CD-ROM, P1.1.

Gilmore, M.S., J.M. Straka, and E.N. Rasmussen, 2004: Precipitation uncertainty due to variations in precipitation particle parameters within a simple microphysics scheme. *Mon. Wea. Rev.*, 2004, **132**, 2610-2627.

Heinselman, P., D. Priegnitz, K. Manross, T. Smith, and R. Adams, 2008: Rapid sampling of severe storms by the National Weather Radar Testbed

- Phased Array Radar. *Wea. Forecasting*, in press.
- Jung, Y., M. Xue, G. Zhang, and J.M. Straka, 2008: Assimilation of Simulated Polarimetric Radar Data for a Convective Storm Using the Ensemble Kalman Filter. Part II: Impact of Polarimetric Data on Storm Analysis. *Mon. Wea. Rev.*, **136**, 2246–2260.
- Lei, T., M. Xue, T. Yu, and M. Teshiba, 2007: Study on the optimal scanning strategies of phase-array radar through ensemble Kalman filter assimilation of simulated data. *33rd Int. Conf. Radar Meteor.*, Cairns, Australia, Amer. Meteor. Soc., CDROM P7.1.
- Lin, Y.-L., R.D. Farley, and H.D. Orville, 1983: Bulk parameterization of the snow field in a cloud model. *J. Appl. Meteor.*, **22**, 1065-1092.
- Snyder, C. and F. Zhang, 2003: Assimilation of simulated Doppler radar observations with an ensemble Kalman filter. *Mon. Wea. Rev.*, **131**, 1663-1677.
- Tong, M. and M. Xue, 2005: Ensemble Kalman filter assimilation of Doppler radar data with a compressible nonhydrostatic model: OSS experiments. *Mon. Wea. Rev.*, **133**, 1789-1807.
- \_\_\_\_ and \_\_\_\_, 2008: Simultaneous estimation of microphysical parameters and atmospheric state with radar data and ensemble Kalman filter. Part I: Sensitivity analysis and parameter identifiability. *Mon. Wea. Rev.*, **136**, 1630-1648.
- Weisman, M. L. and J. B. Klemp, 1982: The dependence of numerically simulated convective storms on vertical wind shear and buoyancy. *Mon. Wea. Rev.*, **110**, 504-520.
- Whitaker, J. S., and T. M. Hamill, 2002: Ensemble data assimilation without perturbed observations. *Mon. Wea. Rev.*, **130**, 1913-1924.
- Wicker, L. J., and W. C. Skamarock, 2002: Time-splitting methods for elastic models using forward time schemes. *Mon. Wea. Rev.*, **130**, 2088-2097.
- Wood, V. T., R. A. Brown, and D. Dowell, 2008: Simulated WSR-88D Velocity and Reflectivity Signatures of Numerically-Modeled Tornadoes. *J. Atmos. Oceanic Technol.* in review.
- Xue, M., M. Tong, and K.K. Droegemeier, 2006: An OSSE framework based on the ensemble square root Kalman filter for evaluating the impact of data from radar networks on thunderstorm analysis and forecasting. *J. Atmos. Oceanic Technol.*, **23**, 46-66.
- Zhang, F., C. Snyder, and J. Sun, 2004: Impacts of initial estimate and observation availability on convective-scale data assimilation with an ensemble Kalman filter. *Mon. Wea. Rev.*, **132**, 1238-1253.

Table 1. Enhanced VCP 11 scan strategy for scanning storms a) within ~70 km and b) beyond ~70 km from the radar location.

# of Angles	VCP 11	Enhanced VCP 11 (< 70 km)	Enhanced VCP 11 (≥70 km)
1	0.50	0.50	0.50
2	1.45	1.45	1.10
3	2.40	2.40	1.70
4	3.35	3.35	2.40
5	4.30	4.30	3.20
6	5.25	5.25	4.10
7	6.20	6.20	5.10
8	7.50	7.20	6.20
9	8.70	8.20	7.40
10	10.00	9.20	8.70
11	12.00	10.20	10.10
12	14.00	11.70	11.70
13	16.70	13.20	13.50
14	19.50	14.70	15.50
15		16.20	
16		17.70	
17		19.20	
18		20.70	
19		22.20	
20		23.70	

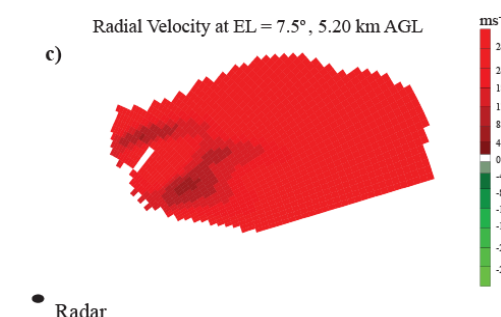
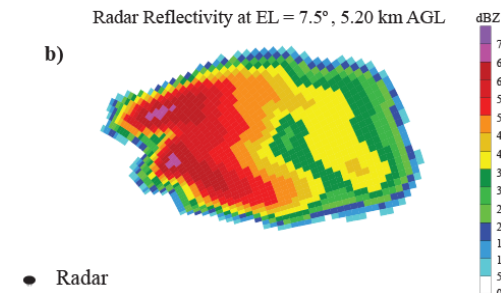
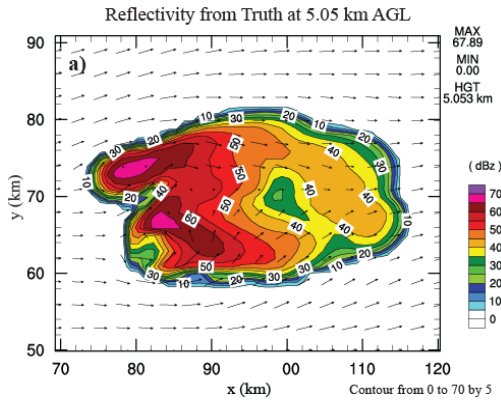
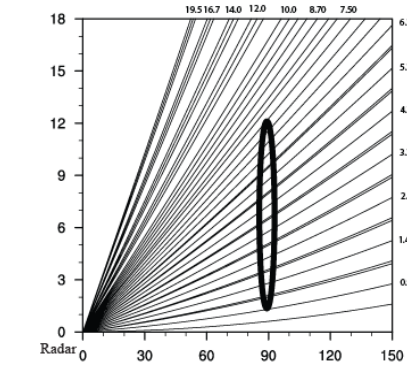
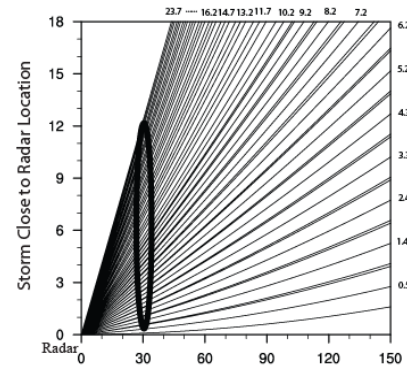


Figure 1. Synthetic radar observations created from (a) the truth run (model reflectivity contours in dBZ and the horizontal wind vectors in  $\text{ms}^{-1}$  at 5.053 km above ground, and the synthetic radar observations of b) reflectivity (dBZ) and c) doppler velocity ( $\text{ms}^{-1}$ ) at  $7.5^\circ$  elevation angle in native radar coordinates at  $t = 39$  min.

a) Regular VCP-11 Number of Scans: 14 Beam Width: 0.89



b) Enhanced VCP-11 Number of Scans: 20 Beam Width: 0.89



c) Enhanced VCP-11 Number of Scans: 14 Beam Width: 0.89

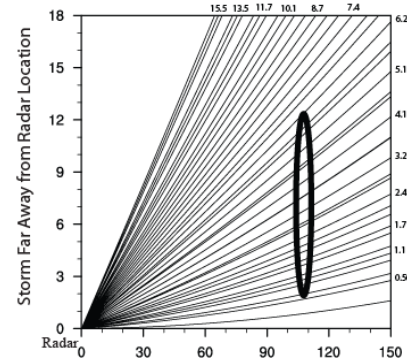


Figure 2. Radar scan angles for a) conventional VCP-11 with 14 scans, b) Enhanced VCP-11 with 20 scans and c) Enhanced VCP-11 with 14 scans. The black vertically stretched ellipsoid indicates the approximate location of the supercell at the last assimilation cycle.

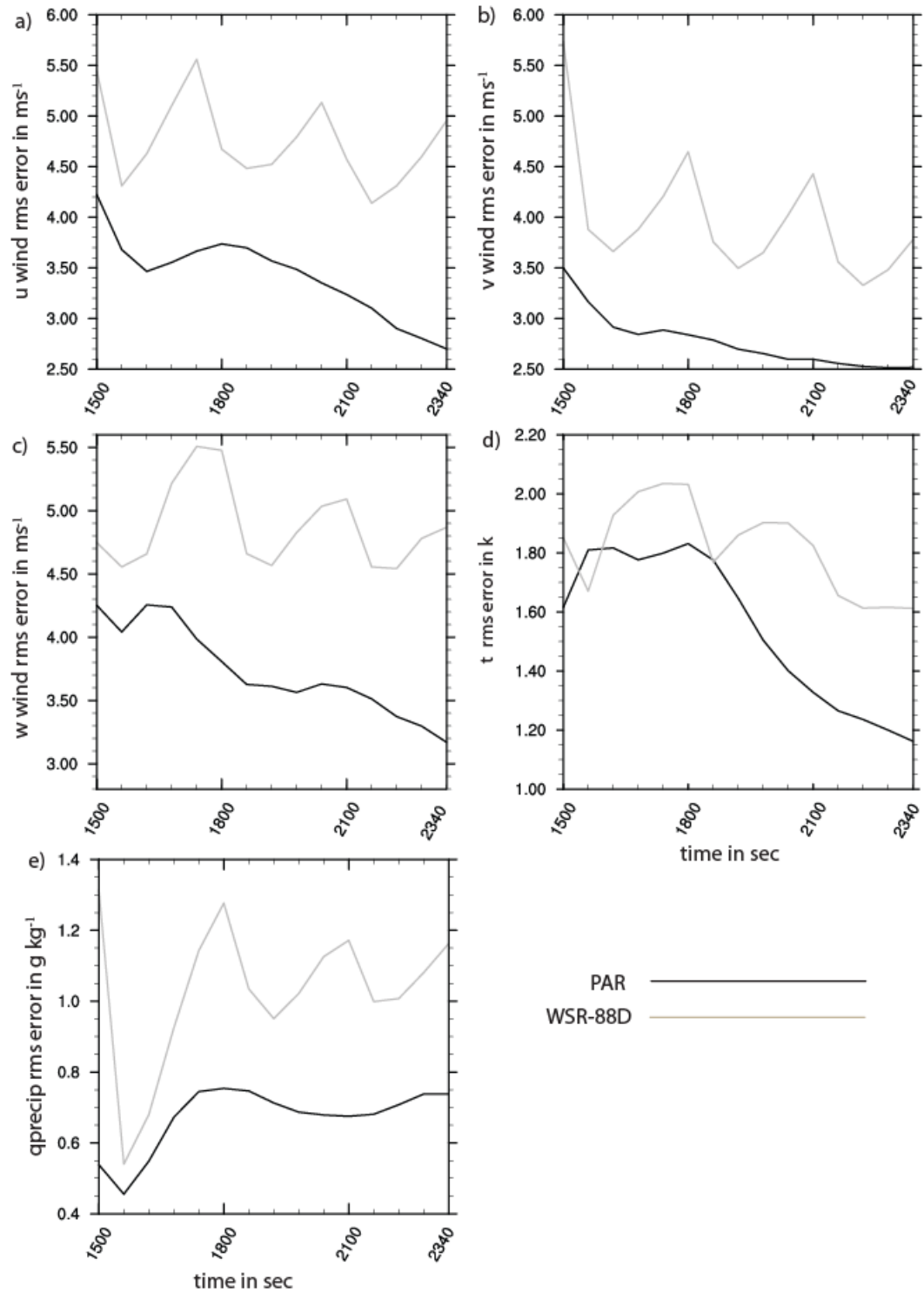


Figure 3. The rms errors of ensemble mean analyses vs. time(s) for the 15-min assimilation experiment for (a)  $u$  ( $\text{ms}^{-1}$ ), (b)  $v$  ( $\text{ms}^{-1}$ ), (c)  $w$  ( $\text{ms}^{-1}$ ), (d)  $t$  (k) and (e) total precipitation mixing ratios ( $\text{g kg}^{-1}$ ) for PAR (black lines) and WSR-88D (gray lines) observations assimilation. Values are averaged over the domain at grid points where the total precipitation mixing ratios (sum of  $q_r$ ,  $q_h$  and  $q_s$ ) is greater than  $0.10 \text{g kg}^{-1}$ . Note that  $300\text{s} = 5 \text{min}$ .

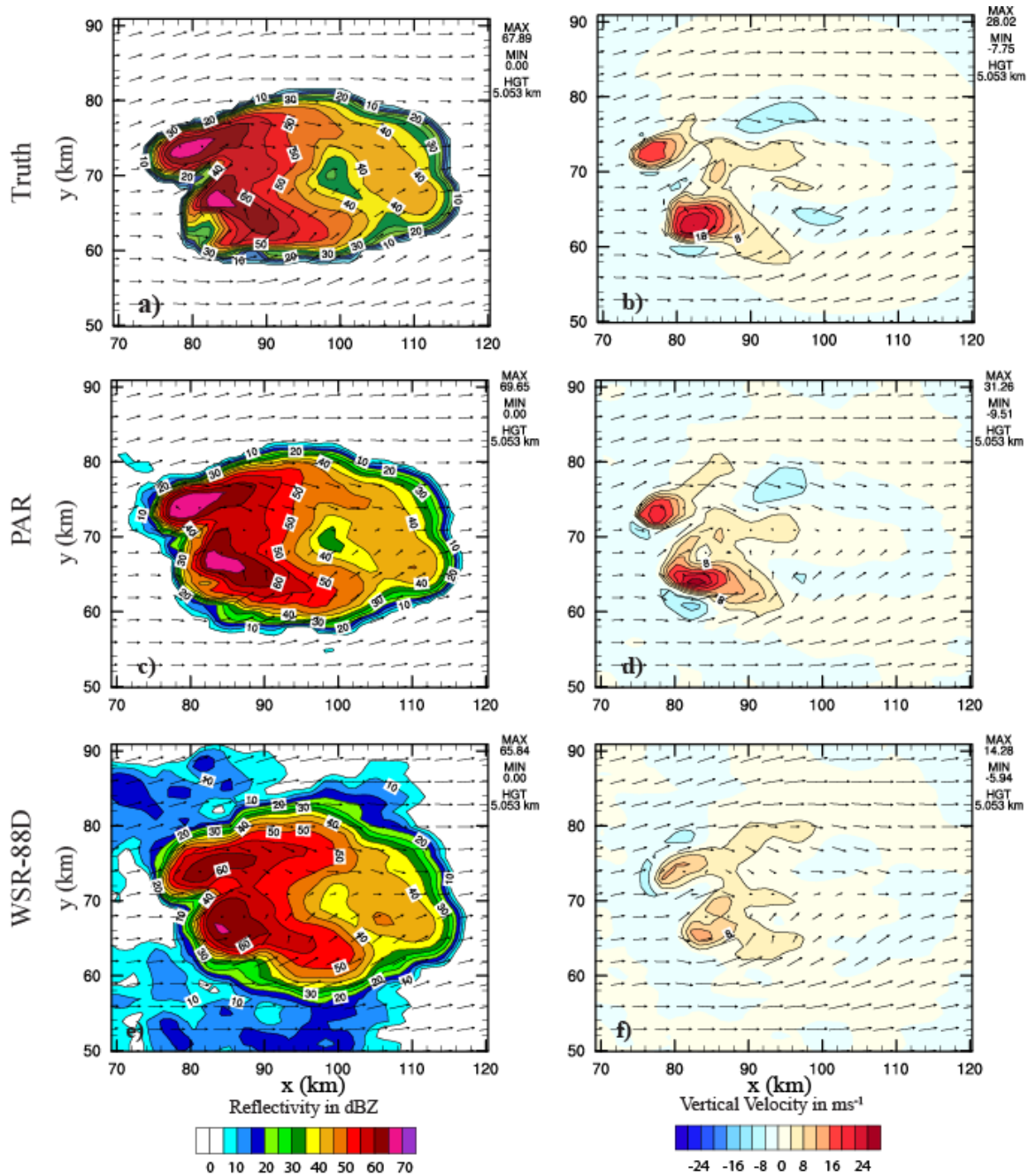


Figure 4. Reflectivity and vertical velocity contours at 5.053 km above ground at the last assimilation cycle ( $t=39$  min) for the 15-min assimilation experiment from (a and b) truth run and ensemble mean analyses from (c and d) PAR observations and (e and f) WSR-88D observation assimilation.

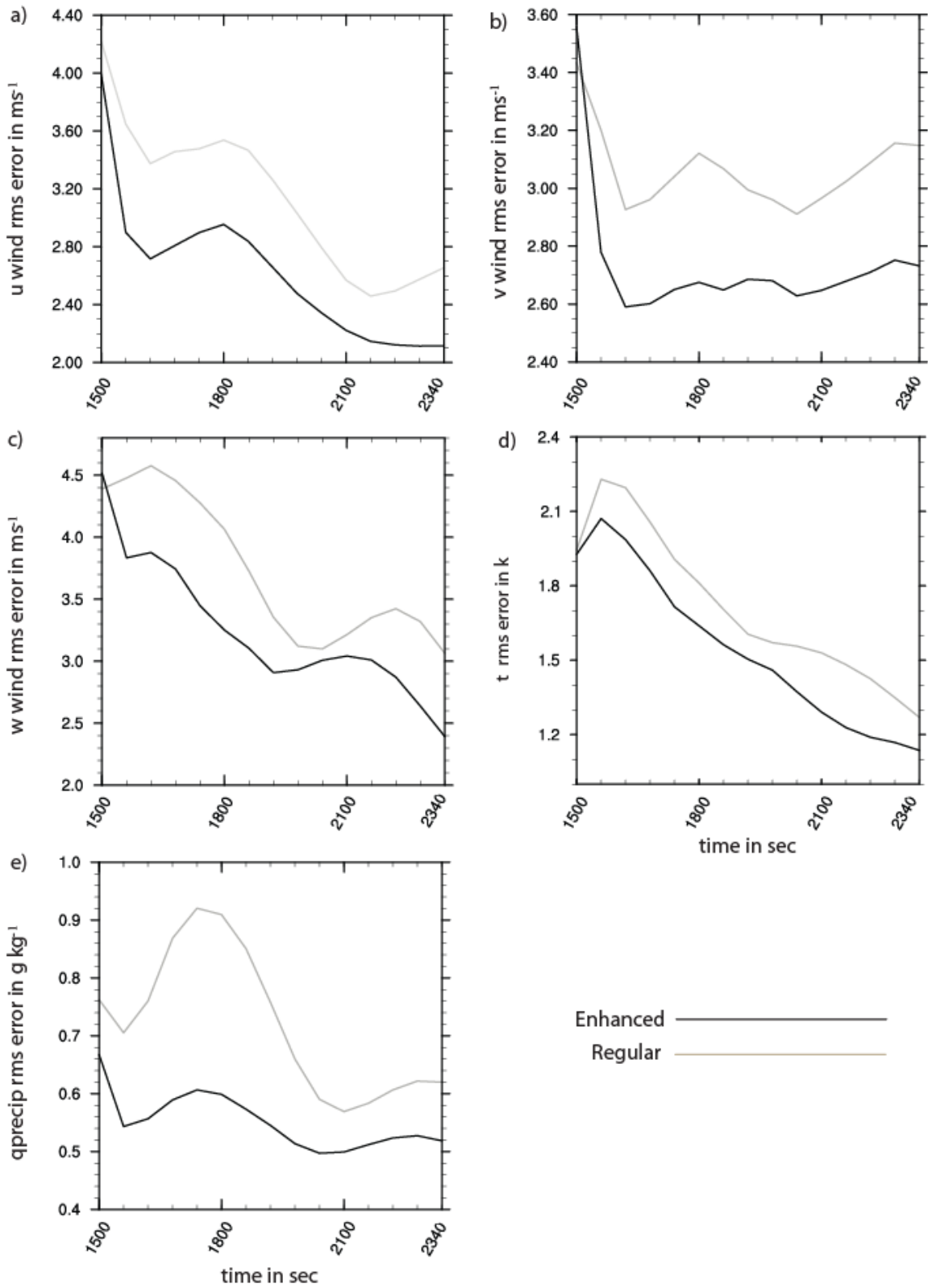


Figure 5. Same as in Fig. 3 but for PAR observation assimilation when the storm is very close to the radar location for regular (gray lines) and enhanced (black lines) scanning strategies.

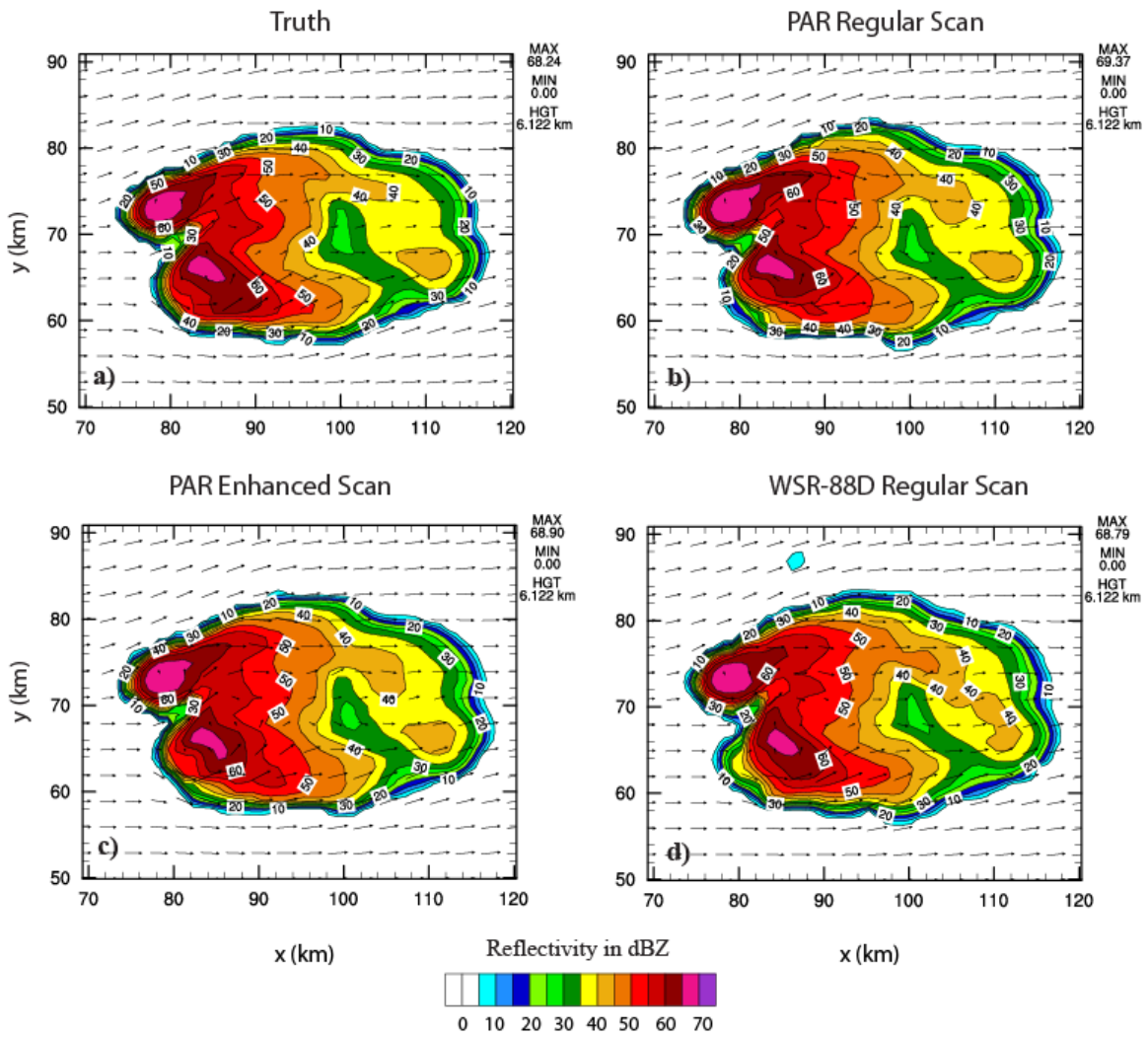


Figure 6. Reflectivity contours at 6.122 km above ground at  $t=39$  min for (a) truth run, ensemble mean analyses at the last assimilation cycle when the radar is very close to the storm from assimilating PAR observations using (b) regular scanning strategy, (c) enhanced scanning strategy and d) WSR-88D observations.

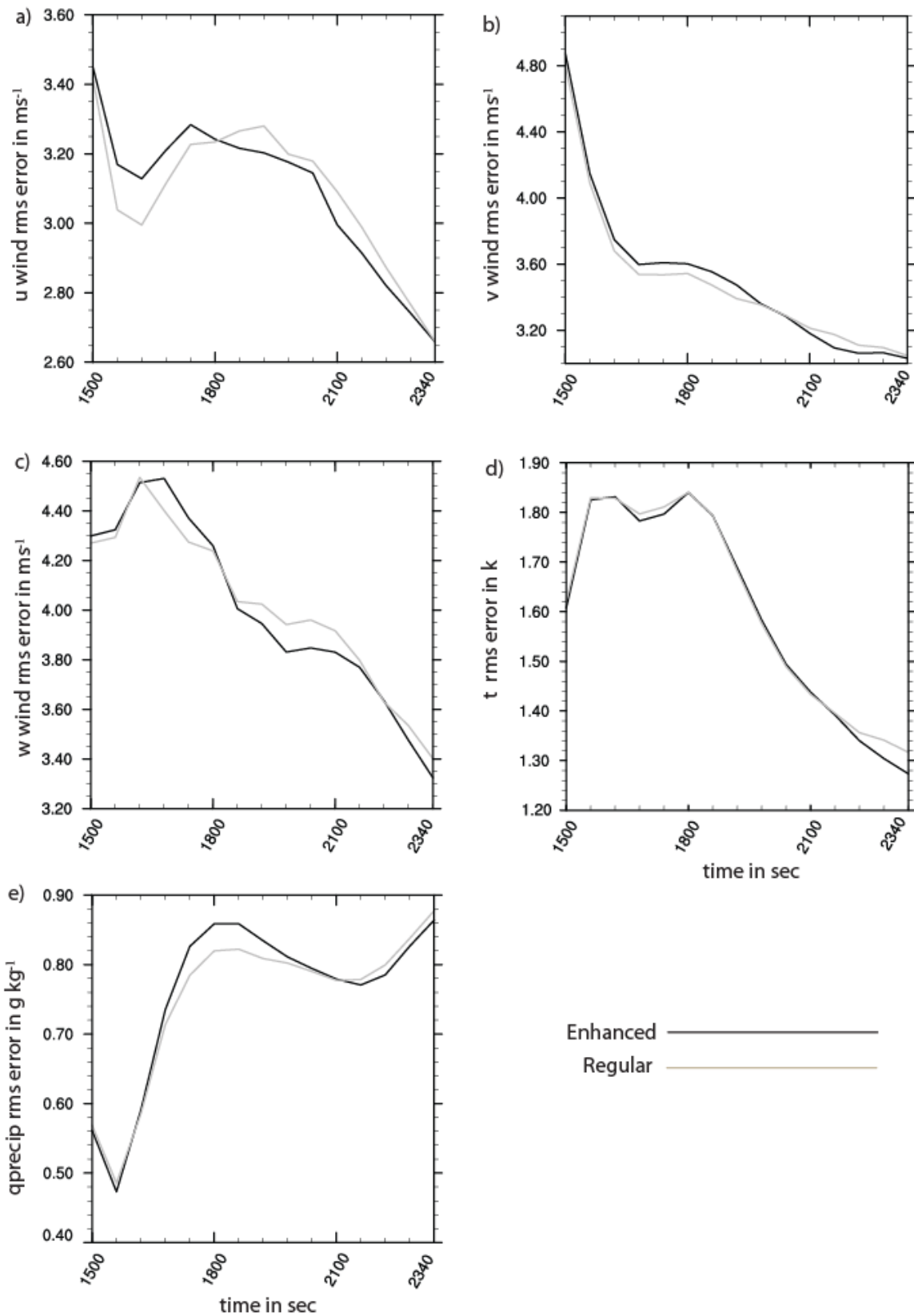


Figure 7. Same as in Fig. 5 but when the storm is far away from the PAR location.

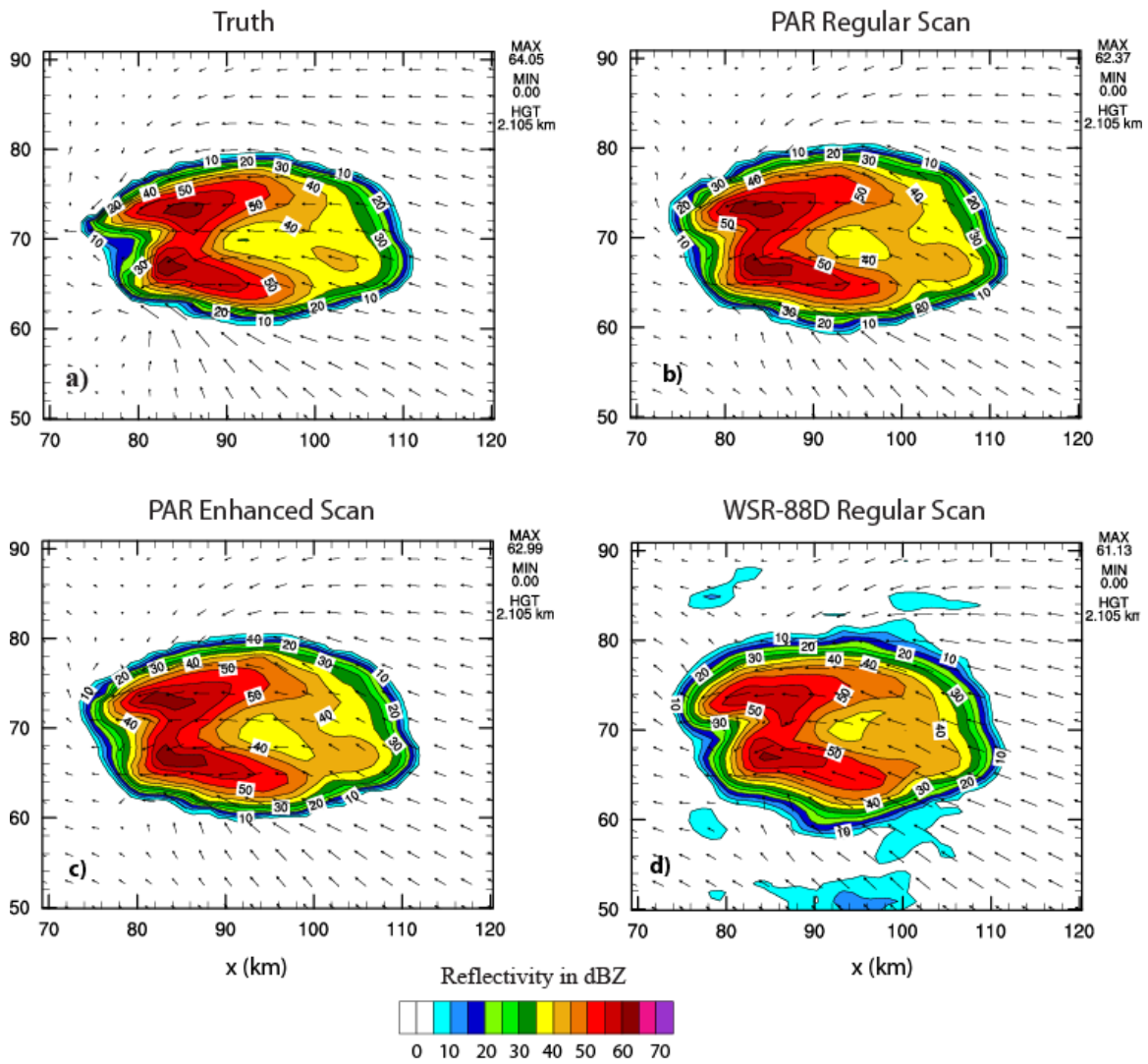


Figure 8. Same as in Fig. 6 but when the radar is far away from storm.

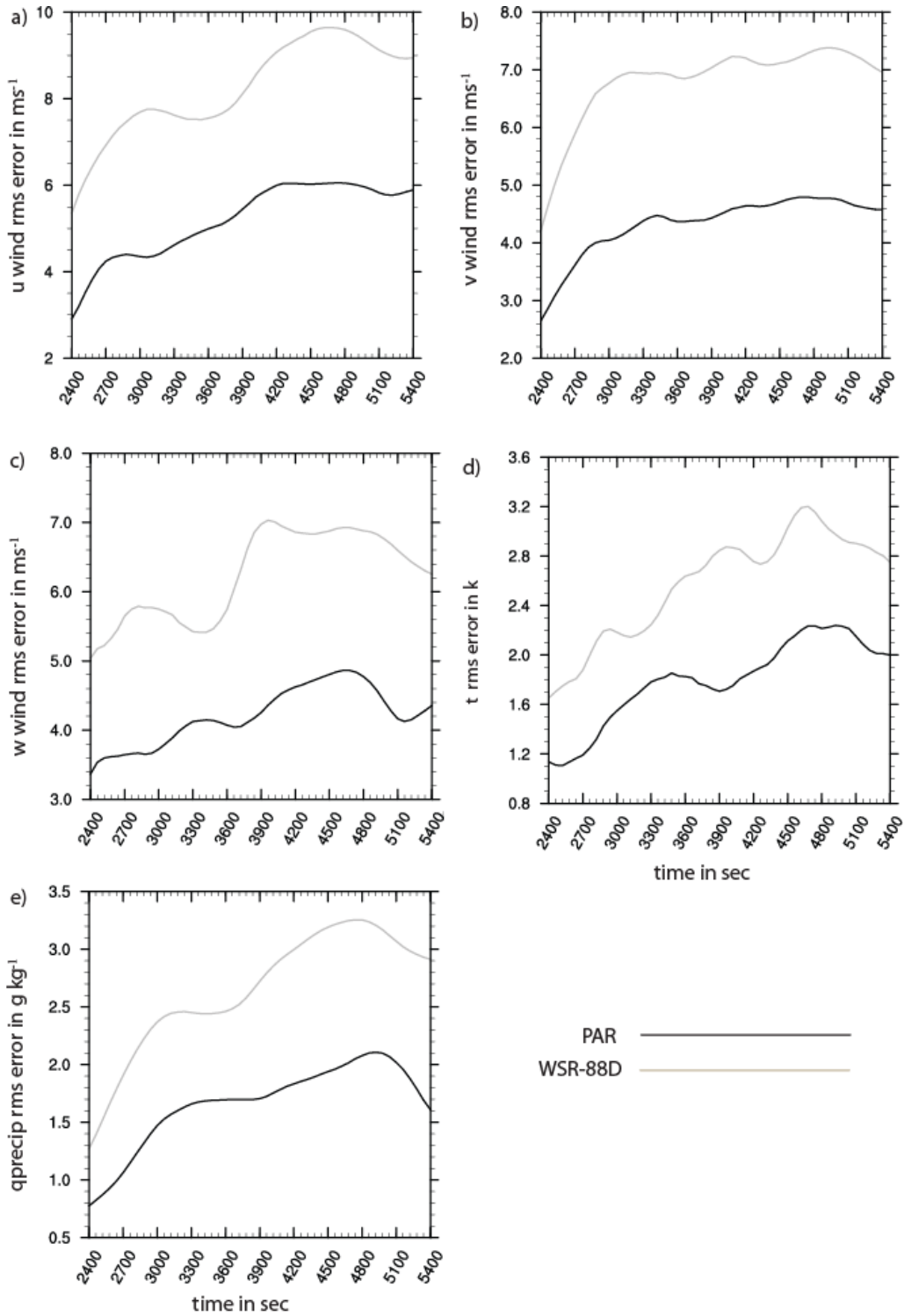


Figure 9. The rms errors of ensemble mean forecast from the 15-min assimilation experiment during the 50-min forecast period for (a)  $u$  ( $\text{ms}^{-1}$ ), (b)  $v$  ( $\text{ms}^{-1}$ ), (c)  $w$  ( $\text{ms}^{-1}$ ), (d)  $t$  (k) and (e)  $q$  ( $\text{g kg}^{-1}$ ). Values are averaged over the domain where the total precipitation (sum of  $q_r$ ,  $q_h$  and  $q_s$  mixing ratios) is greater than  $0.10 \text{g kg}^{-1}$ . Details are shown in the legend.

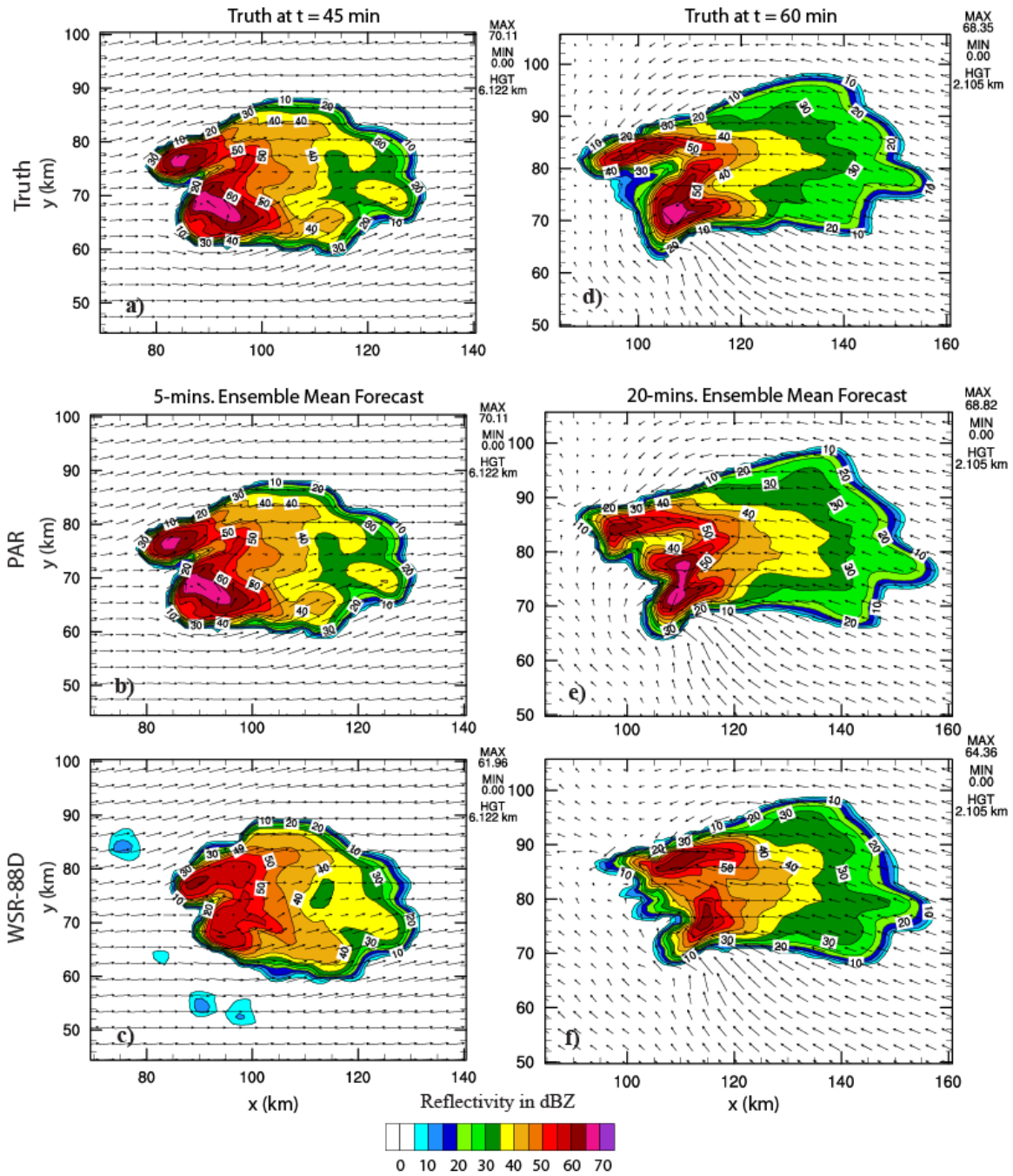


Figure 10. Reflectivity contours for (a and d) truth and forecasts from the 15-min assimilation experiment from (b and e) PAR observations assimilation and (c and f) WSR-88D observations assimilation. (b) and (c) are 5 min ensemble mean forecast while (e) and (f) are 20 min ensemble mean forecasts.

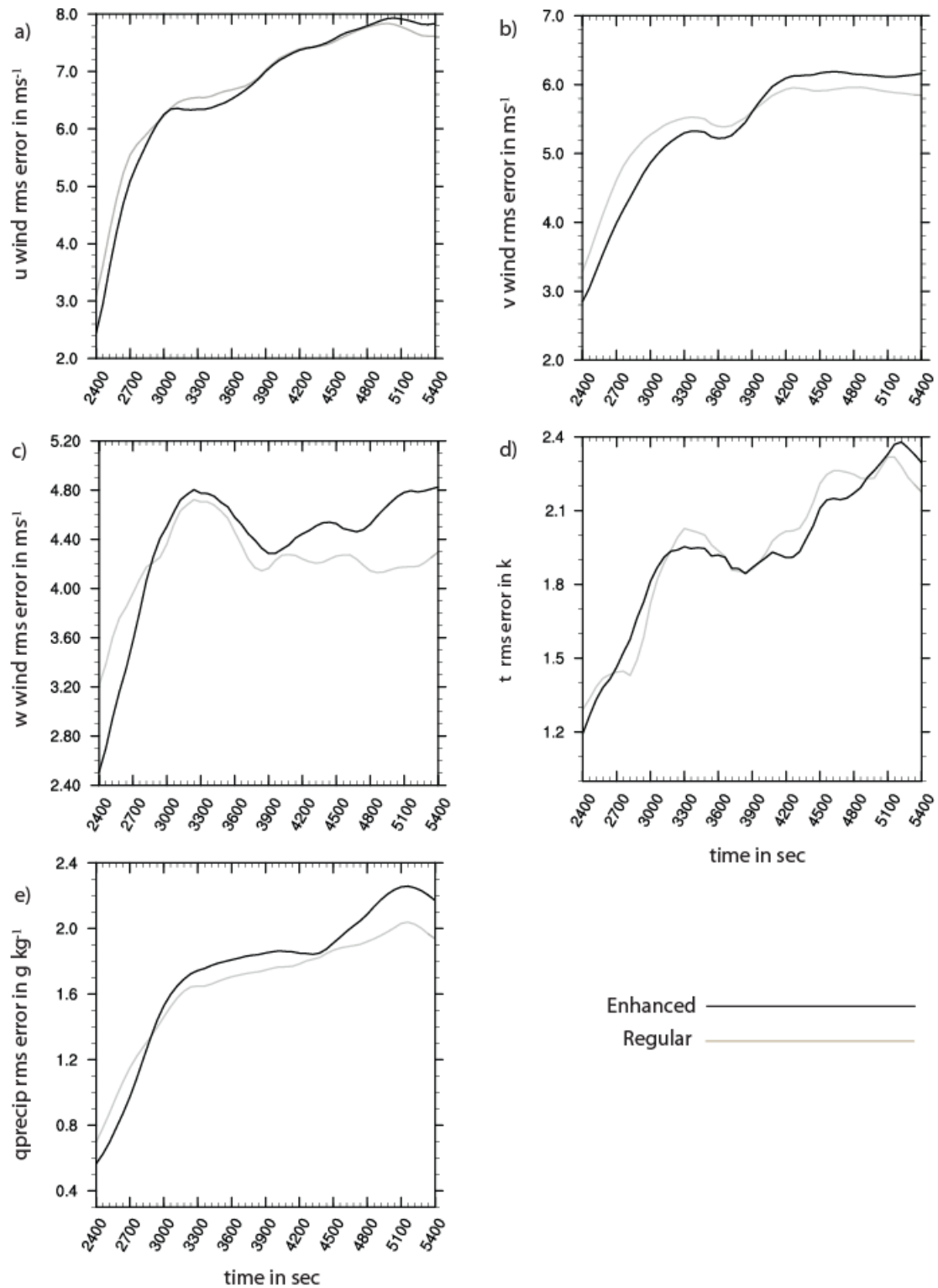


Figure 11. Same as in Fig.9 but for ensemble mean forecast rms error from PAR observation assimilation when the storm is very close to the radar. The rms errors from regular PAR observation are shown in gray and the enhanced PAR observation is shown in black.

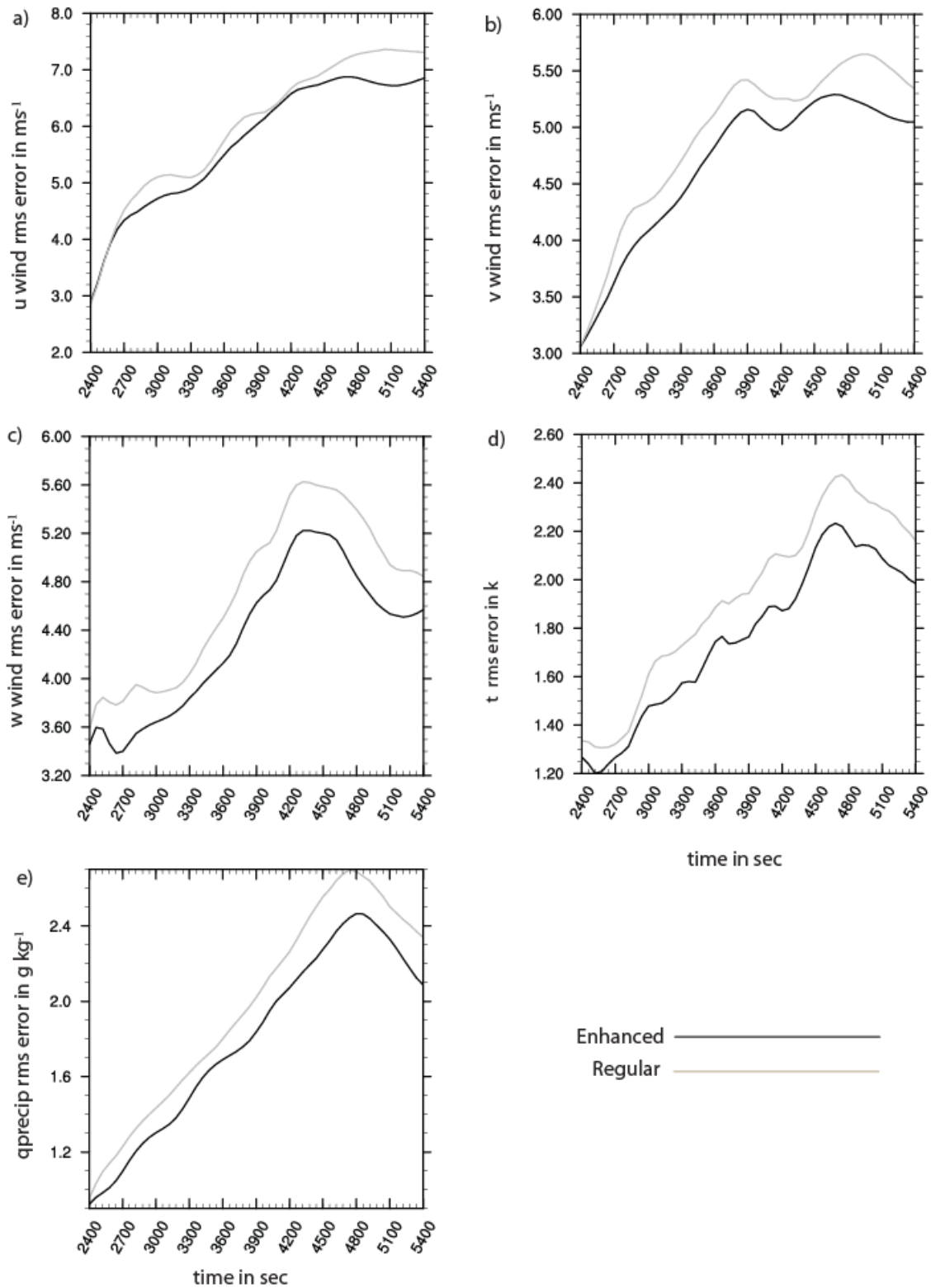


Figure 12. Same as in Fig.11 but for ensemble mean forecast rms error from PAR observation assimilation when the storm is far away from the radar.